



HAL
open science

Relations between oxidation induced microstructure and mechanical durability of oxide scales

Valérie Parry, Céline Pascal, Muriel Braccini, Elena Fedorova, Marc Mantel, Yves Wouters, Djar Oquab, Daniel Monceau, Rafael Estevez, Guillaume Parry

► To cite this version:

Valérie Parry, Céline Pascal, Muriel Braccini, Elena Fedorova, Marc Mantel, et al.. Relations between oxidation induced microstructure and mechanical durability of oxide scales. *Oxidation of Metals*, 2017, 88 (1-2), pp.29-40. 10.1007/s11085-016-9673-5 . hal-01579556

HAL Id: hal-01579556

<https://hal.science/hal-01579556>

Submitted on 31 Aug 2017

HAL is a multi-disciplinary open access archive for the deposit and dissemination of scientific research documents, whether they are published or not. The documents may come from teaching and research institutions in France or abroad, or from public or private research centers.

L'archive ouverte pluridisciplinaire **HAL**, est destinée au dépôt et à la diffusion de documents scientifiques de niveau recherche, publiés ou non, émanant des établissements d'enseignement et de recherche français ou étrangers, des laboratoires publics ou privés.



Open Archive TOULOUSE Archive Ouverte (OATAO)

OATAO is an open access repository that collects the work of Toulouse researchers and makes it freely available over the web where possible.


This is an author-deposited version published in: <http://oatao.univ-toulouse.fr/>
Eprints ID : 18118

To link to this article: DOI: 10.1007/s11085-016-9673-5
URL: <http://dx.doi.org/10.1007/s11085-016-9673-5>

<p>To cite this version: Parry, Valérie and Pascal, Céline and Braccini, Muriel and Fedorova, Elena and Mantel, Marc and Wouters, Yves and Oquab, Djar and Monceau, Daniel and Estevez, Rafael and Parry, Guillaume <i>Relations between oxidation induced microstructure and mechanical durability of oxide scales.</i> (2017) Oxidation of Metals, vol. 88 (n° 1-2). pp. 29-40. ISSN 0030-770X</p>

Any correspondence concerning this service should be sent to the repository administrator: staff-oatao@listes-diff.inp-toulouse.fr

Relations Between Oxidation Induced Microstructure and Mechanical Durability of Oxide Scales

Valérie Parry¹  · Céline Pascal¹ · Muriel Braccini¹ ·
Elena Fedorova^{2,3} · Marc Mantel^{1,4} ·
Yves Wouters¹ · Djar Oquab³ · Daniel Monceau³ ·
Rafael Estevez¹ · Guillaume Parry¹

Abstract Most industrial heat-resistant stainless steels contain silicon as a minor constituent. At high temperature, the internal formation of amorphous silica reduces oxidation rates but decreases the metal/oxide interface toughness. Tensile testing experiments performed on AISI 304L previously oxidized in synthetic air for 50 h at 900 or 1000 °C showed a relation between the silica morphology and location and the crack patterns. A micromechanical modeling using cohesive zone models to describe interfaces fracture behavior is proposed to investigate relevant parameters controlling the silica/alloy interface debonding. Calculations carried out using the

✉ Valérie Parry
valerie.parry@simap.grenoble-inp.fr

Céline Pascal
celine.pascal@simap.grenoble-inp.fr

Muriel Braccini
muriel.braccini@simap.grenoble-inp.fr

Elena Fedorova
fedorova.elena.85@gmail.com

Marc Mantel
marc.mantel@ugitech.com

Yves Wouters
yves.wouters@simap.grenoble-inp.fr

Djar Oquab
djar.oquab@ensiacet.fr

Daniel Monceau
daniel.monceau@ensiacet.fr

Rafael Estevez
rafael.estevez@simap.grenoble-inp.fr

Guillaume Parry
guillaume.parry@simap.grenoble-inp.fr

finite elements method have shown that location of silica inclusions and silica/metal interface toughness are key parameters determining the cracks pattern morphology and the critical strain at failure.

Keywords AISI 304L · Tensile testing · Silica embrittlement · Micromechanical modeling

Introduction

Long-term oxidation resistance of heat-resistant alloys is often a compromise between chemical and mechanical aspects. Decreasing the oxidation rate and maintaining good adhesion of the protective oxide layer to the bulk surface is crucial for life time improvement. Most of the industrial stainless steels contain silicon, at a level of 0.5 wt% for ferritic grades, up to 2 wt% for austenitic grades. In terms of oxidation behavior, the optimum value lies at 1 wt% for austenitic grades with parabolic rate constants at 900 °C reduced by a factor of three compared to grades with no silicon [1].

It is known that the internal formation of amorphous silica precipitates inhibits chromium supply to the chromia scale which reduces oxidation rates [1–6]. However, the brittle character of the grown silica is detrimental to the metal/oxide interface toughness. It is generally observed that adhesion of chromia decreases with increasing silicon content, with severe spallation when a continuous silica film is formed at the steel/chromia interface [1, 5, 6]. However, for austenitic stainless steels oxidized above 800 °C, the accelerated inward interfacial diffusion of oxygen results in silica internal oxidation along the grain boundaries [7]. In a previous paper, we have shown that internal oxidation of Si along the grain boundaries modifies the damaging behavior of the oxide scale [8].

The objectives of the present work are to understand the relation between, on the one hand, the silica morphology and location, and on the other hand, the mechanical behavior of the oxidation-affected zone. The experimental part focuses on the relation between the silica microstructure and crack patterns obtained during SEM in situ tensile testing after oxidation of AISI 304L in synthetic air for 50 h at 900 or 1000 °C. A micromechanical modeling using cohesive zone models to describe interfaces fracture behavior is proposed to investigate relevant parameters controlling the silica/alloy interface debonding. Calculations are carried out using the finite elements method.

¹ Univ. Grenoble Alpes, CNRS, SIMaP, 38000 Grenoble, France

² Polytechnic Institute of Siberian Federal University, Krasnoyarsk, Russia

³ CIRIMAT Laboratory, University of Toulouse, CNRS, INPT, UPS, ENSIACET 4 allée Emile Monso, BP-44362, 31030 Toulouse Cedex 4, France

⁴ UGITECH SA, Ugine, France

Experimental Procedures

Austenitic stainless steel AISI 304L (Fe–18.0 Cr–8.96 Ni–1.13 Mn–0.46 Si wt%) with grain size around 15–20 μm provided by Ugitech was chosen as substrate. Details of alloy production and composition are described in [8, 9]. Samples were obtained from 22 mm diameter rod. Rectangular plates (1-mm thick) were cut in the longitudinal direction by electrical discharge machining and ground with SiC paper down to a final grade of P1200. Tensile specimens were machined from these plates using electrical discharge machining. Their geometry presents a gauge section of 2 mm width by 1-mm thick and a gauge length of 3 mm [8]. Prior to oxidation, samples were cleaned in an ultrasonic bath with acetone followed by high-purity ethanol.

Tensile specimens were oxidized in a tubular furnace for 50 h in synthetic air with a flow rate of 0.6 l h^{-1} . The temperature was set at either 900 or 1000 $^{\circ}\text{C}$. The heating rate was set to 60 $^{\circ}\text{C min}^{-1}$.

Oxidized tensile specimens were loaded into a homemade micromechanical device adapted into a JEOL JSM 6400 scanning electron microscope (SEM). This device permits the continuous observation at a microscopic scale of mechanical damages, such as cracking and spalling, at the surface of the oxide layer. A displacement rate of 50 $\mu\text{m min}^{-1}$ was chosen. Additional information on the tensile testing experimental procedure is available in [8, 10].

In order to characterize the oxidation-affected zone in the substrate beneath the oxide scale before and after tensile testing, the oxide scale was chemically or mechanically removed. Surface polishing was performed on as oxidized samples whereas chemical etching for 4 h in ($\text{KMnO}_4 + \text{NaOH}$) solution at 90 $^{\circ}\text{C}$ was performed on oxidized samples after tensile testing. Surface observations were performed with an optical microscope and a scanning electron microscope (SEM) FEG ZEISS ULTRA 55 in secondary electron (SE) mode.

After tensile testing, the oxidized samples were cross-sectioned and prepared for metallographic analysis using conventional techniques, i.e. grinding, polishing and fine polishing. Prior to mounting, the samples were coated with a thin epoxy resin layer to protect the oxide scale and the crack pattern. The morphology and microstructure of the oxide scale and the oxidation-affected zone of the strained samples were characterized using a SEM FEG ZEISS ULTRA 55 equipped with EDS analysis in backscattered electron (BSE) mode. Thickness measurements were performed on SEM cross sections using Fiji-ImageJ software [11].

Results and Discussion

Experimental Results

Figure 1a and b shows optical micrographs of the oxidation-affected zones after 50 h at 900 and 1000 $^{\circ}\text{C}$ respectively. The presence of remaining spots of oxide scale on the surface indicates that the observed areas were located right beneath the

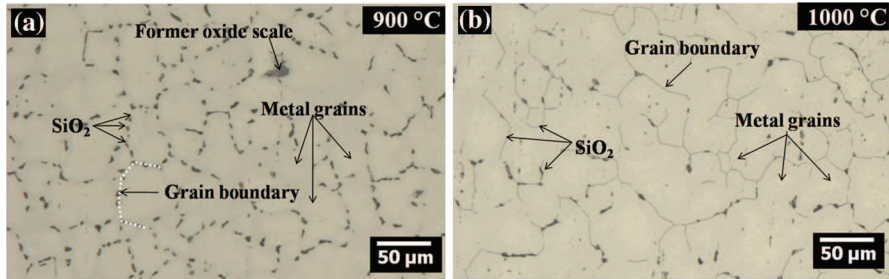


Fig. 1 Optical micrographs of the oxidation-affected zones, beneath the oxide scale, grown on AISI 304L oxidized for 50 h in synthetic air at **a** 900 °C and **b** 1000 °C. The oxide scale was removed by surface polishing

oxide scale. For both temperatures, the metal grain size is around 40 μm indicating grain growth during oxidation. Sub-surface observations reveal internal oxidation, appearing in black. After oxidation at 900 °C, strings of small precipitates decorate the substrate grain boundaries (Fig. 1a) whereas at 1000 °C, formation of oxide occurs as a thin and continuous network along the grain boundaries (Fig. 1b).

Figure 2 shows SEM surface views in SE mode showing the crack pattern (a)(c) and cracks details (b)(d) after tensile testing performed on AISI 304L oxidized for 50 h at 900 °C (for 63% strain) and 1000 °C (for 43% strain), respectively. In order to highlight the crack paths, the oxide scale of the 1000 °C

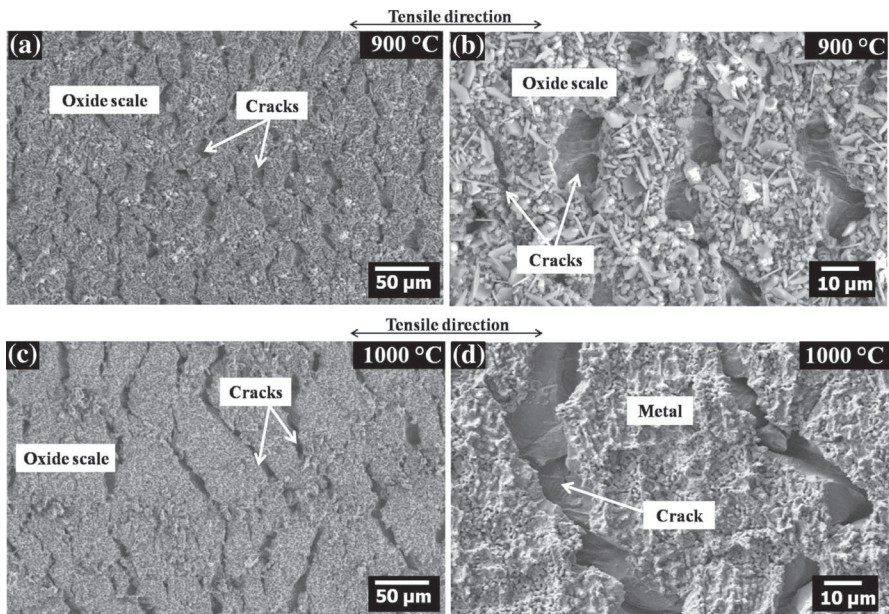


Fig. 2 SEM top surface views of the oxide scale in SE mode after tensile testing performed on AISI 304L oxidized for 50 h in synthetic air at 900 °C (63% strain): **a** crack pattern and **b** crack details and at 1000 °C (43% strain): **c** crack pattern and **d** crack details after chemical etching to remove oxide scale

sample was removed by chemical etching in ($\text{KMnO}_4 + \text{NaOH}$) solution at $90\text{ }^\circ\text{C}$ for 4 h (Fig. 2d).

Two key features of the crack patterns can be noticed. First, no spallation occurs, even for large strain ratio. Second, the cracks remain perpendicular to the tensile direction, whereas they do not propagate straight as usually observed [12]. It has been shown in [8] that during tensile testing, cracks open due to the ductile deformation of the underneath substrate. This results in wide cracks formation with bare metal appearance at the cracks roots as seen in Fig. 2b. For the sample oxidized at $1000\text{ }^\circ\text{C}$, cracks are longer and present chevron-like shape. For the sample oxidized at $900\text{ }^\circ\text{C}$, it can be noticed that for a few cracks plastic deformation of the metal at the crack root does not occur (see left arrow in Fig. 2b).

SEM cross sections and EDS maps after tensile testing of oxide scales thermally grown on AISI 304L for 50 h at $900\text{ }^\circ\text{C}$ or $1000\text{ }^\circ\text{C}$ are shown in Figs. 3 and 4 respectively. After tensile testing, the metal/oxide interfaces remain adhesive with no evidence of oxide scale spallation. The metal/oxide interfaces are undulated and the oxide scales are continuous. Oxide scales thicknesses are about $2.5 \pm 0.5\ \mu\text{m}$ and $4 \pm 1\ \mu\text{m}$ after oxidation at 900 and $1000\text{ }^\circ\text{C}$ respectively. A duplex structure is evidenced by EDS mapping and corresponds to the well-described regular situation: a $(\text{Mn,Cr})_3\text{O}_4$ spinel top layer and Cr_2O_3 rich inner layer [9, 13, 14]. At $1000\text{ }^\circ\text{C}$, the outer spinel layer is continuous, characterized by large micro-crystallized grains inducing variations in scale thickness.

Formation of needle-like internal precipitates of SiO_2 is also observed. This result can be related to the intergranular oxidation patterns as shown in Fig. 1. The growth of SiO_2 along the grain boundaries of austenitic stainless steels oxidized above $800\text{ }^\circ\text{C}$ has already been observed in literature [2, 8–10]. The morphology and size of the oxide particles are linked to the accelerated inward interfacial diffusion of oxygen along the interfaces between internal oxides and the alloy grains compared to lattice diffusion in the substrate. This results in the formation of needle-like precipitates with deep penetrations. The temperature is known to affect diffusion processes and then the oxide growth rate so that particle size increases with increasing temperature [7].

At $900\text{ }^\circ\text{C}$, intergranular precipitation of silica is discontinuous and characterized by strings of small individual particles (Fig. 1a), with a penetration depth of about $6 \pm 1\ \mu\text{m}$ (Fig. 3a). After a $1000\text{ }^\circ\text{C}$ thermal treatment, intergranular oxidation of Si occurs as a thin and continuous network encompassing several grain boundaries

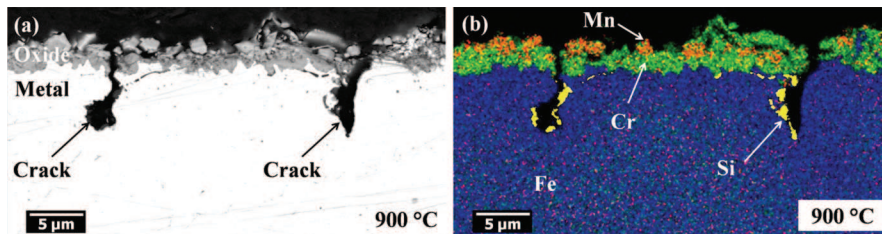


Fig. 3 a SEM cross-section in BSE mode and b EDS map, after tensile testing performed on AISI 304L oxidized for 50 h in synthetic air at $900\text{ }^\circ\text{C}$ (63% strain)

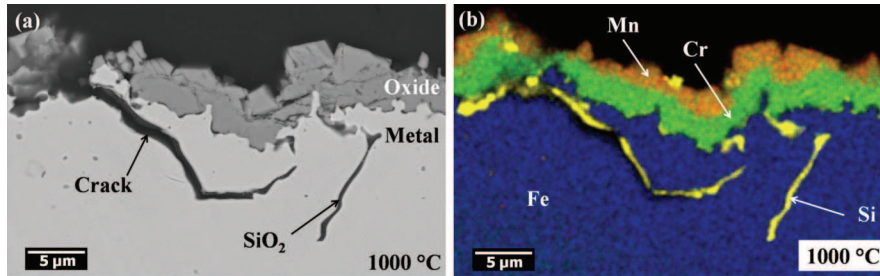


Fig. 4 **a** SEM cross-section in BSE mode and **b** EDS map, after tensile testing performed on AISI 304L oxidized for 50 h in synthetic air at 1000 °C (43% strain)

(Fig. 1b). The penetration depth reaches $12 \pm 2 \mu\text{m}$ (Fig. 4a), about two times the penetration depth obtained after oxidation at 900 °C.

In a former paper dedicated to results obtained on samples oxidized at 1000 °C [8], it was shown that internal oxidation of Si plays a key role on the overall mechanical behavior during tensile testing. In summary, the cracks in the oxide scale were linked to the silica embrittlement of the grain boundaries in the underneath substrate. It was also observed that the localized plastic deformation of the metal at the crack root decreases the strain transferred to the oxide film preventing oxide scale spallation.

In the present study, temperature dependence is evidenced. The difference between crack patterns observed at 900 and 1000 °C are related to silica morphology and location. During tensile testing, strings of small SiO_2 precipitates generate short cracks (900 °C case), whereas a thin and continuous network of silica along the grain boundaries induces long chevron-like cracks (1000 °C case).

Micromechanical Modeling

In order to investigate relevant parameters controlling the silica/alloy debonding, a micromechanical modeling is proposed. A 2D plane strain framework is considered. The following geometrical parameters of the oxidation-affected zone are considered: size, morphology and distance between inclusions, thickness of the oxide scale and cracks formation through the oxide scale. The geometry of the model is shown in Fig. 5 and the dimensional geometric parameters estimated based on the experiment performed at 900 °C for 50 h, are summarized in Table 1. The interfaces were assumed to be flat. The width W of the model is set to the mean distance between two silica inclusions. The thickness ratio H/h between the oxide scale and the bulk is 30. A crack formation in the oxide scale is considered. Two crack/inclusion distances d were studied: 1.7 μm and 3.9 μm . The first one is the “close crack geometry” and corresponds to one-sixth of the distance between two inclusions. The “remote crack geometry” will refer to the second one and is set to one-third of the distance between two inclusions. These two geometries aim at describing fracture behavior observed after tensile testing on the sample oxidized at 900 °C for 50 h. According to Fig. 2, cracks opening due to the ductile deformation

Fig. 5 Schematic sketch of the model

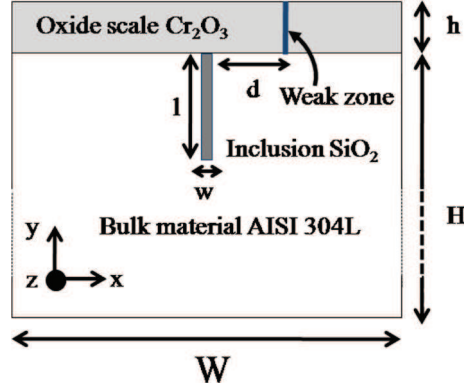


Table 1 Dimensional parameters of the finite element mesh (μm)

Oxide scale		Inclusion		Metal	
Thickness (h)	2.4	Length (l)	5.7	Thickness (H)	72
Crack/inclusion distance (d)	1.7 or 3.9	Width (w)	0.6	Width (W)	25.6

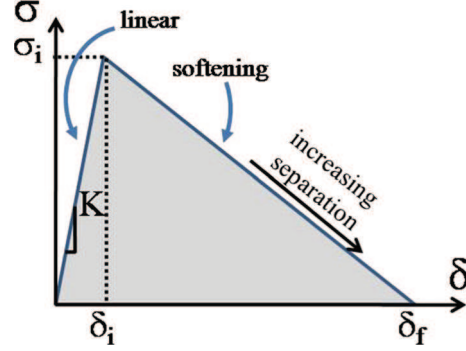
of the underneath substrate is mainly observed whereas for a few cracks, plastic deformation of the metal at the crack root does not occur. The loading consists of an applied displacement U on the right edge of the cell in direction x , resulting in a nominal applied strain $\varepsilon_0 = U/W$.

Material data are shown in Table 2. For the oxide scale, we consider an elastic film with the mechanical properties of Cr_2O_3 [15]. The inclusion is related to SiO_2 and has a pure elastic behavior [16]. The metallic substrate has an elastic–plastic behavior. A plasticity model based on the Von Mises criterion (J_2 plasticity) with isotropic hardening is chosen. The hardening is calibrated based on the stress–strain curve of the tensile testing. In order to account for cracks initiation and propagation at interfaces and in the oxide scale, a cohesive zone model is used [17, 18]. The constitutive behavior of interfaces consists of a traction versus separation law is presented in Fig. 6. Due to interaction between the two separating faces, the traction $\bar{\sigma}$ depends upon the separation vector $\bar{\delta}$, which is the relative displacement between opposite crack faces at a point initially joined on the interface. The separation and

Table 2 Material data for the micromechanical model

Section	Material	Mechanical properties	
		Young's modulus (GPa)	Poisson's ratio
Oxide scale	Cr_2O_3	230	0.25
Inclusion	SiO_2	72	0.17
Metal	AISI 304L	190	0.29

Fig. 6 Traction versus separation law describing interface fracture behavior



traction vectors can be resolved into their normal components (δ_n, σ_n), the opening or mode I contribution, and their tangential components resolved in the direction normal to the crack front (δ_t, σ_t), the shearing or mode II contribution.

A mixed-mode traction versus separation law is described through a linear/softening model. According to Fig. 6, prior to attaining the peak traction, the traction–separation relation is linear and reversible:

$$\bar{\sigma} = K\bar{\delta} \quad (1)$$

with K being the stiffness. For any combination of traction components (σ_n, σ_t), peak values (σ_n^i, σ_t^i) related to crack initiation in the cohesive zone model, are reached when:

$$\left(\frac{\sigma_n}{\sigma_n^{\max}}\right)^2 + \left(\frac{\sigma_t}{\sigma_t^{\max}}\right)^2 = 1 \quad (2)$$

where σ_n^{\max} is the maximum traction in mode I and σ_t^{\max} is the maximum traction in mode II. The corresponding separations at the peaks are $\bar{\delta}^i = (\delta_n^i, \delta_t^i)$. Once peak traction is attained, softening sets which results in decreasing traction (see Fig. 6). The separation energy or interfacial toughness G_c is the area under the curve.

Cohesive zones were assigned to the metal/oxide (MO) and to the metal/inclusion (MI) interfaces and to the crack considered in the oxide scale (Ox). The positions of the cohesive zones in the finite element model are shown in Fig. 7. Maximum tractions ($\sigma_{n,\alpha}^{\max}, \sigma_{t,\alpha}^{\max}$) and separation energies ($G_{c,\alpha}$) — α refers to MI, MO, or Ox—assigned to the cohesive zones are shown in Table 3. In the following, the maximum traction of the MO interface for mode I contribution $\sigma_{n,MO}^{\max}$ and the separation energy $G_{c,MO}$ are constant and arbitrarily set to 600 MPa and 3 J.m⁻², respectively. The order of magnitude of $\sigma_{n,MO}^{\max}$ and $G_{c,MO}$ is in agreement with literature [17]. The shear coefficient α describing the relation between the shear separation and the normal separation can take an arbitrary value [17]. In the following, this value is set to 5. The value of the initial stiffness K has to be chosen high enough to avoid any excessive artificial elastic opening of the cohesive zone prior to damage initiation. Calculations of the equivalent plastic strain ϵ_p^{eq} during tensile testing are carried out using the finite elements software ABAQUS [19]. Periodic boundaries

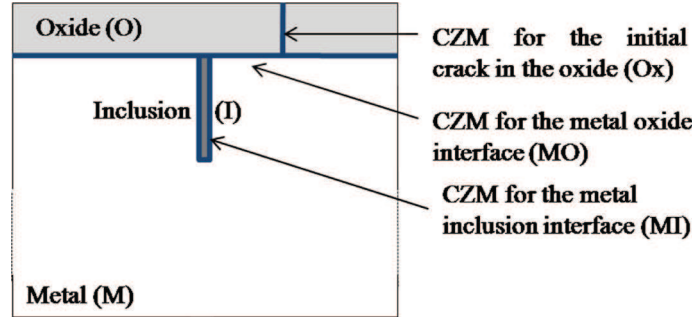


Fig. 7 Positions of the cohesive zone models (CZM) in the finite element model

Table 3 Maximum tractions and separation energies of the metal/oxide (MO) and the metal/inclusion (MI) interfaces and of the crack considered in the oxide scale (Ox)

	Metal/oxide interface (MO)	Metal/inclusion interface (MI)	Oxide/oxide interface (Ox) (initial crack)
$\sigma_{n,MO}^{\max}$	600 MPa	$\sigma_{n,MI}^{\max}$	From 0.1 to 1.5 $\sigma_{n,MO}^{\max}$
$\sigma_{t,MO}^{\max}$	$5\sigma_{n,MO}^{\max}$	$\sigma_{t,MI}^{\max}$	$5\sigma_{n,MI}^{\max}$
$G_{c,MO}$	3 J m^{-2}	$G_{c,MI}$	From 0.5 to 1 $G_{c,MO}$
			$\sigma_{n,Ox}^{\max}$
			From 10^{-3} to 50 $\sigma_{n,MO}^{\max}$
			$\sigma_{t,Ox}^{\max}$
			$5\sigma_{n,Ox}^{\max}$
			$G_{c,Ox}$
			$G_{c,MO}$

conditions are used. Attention is paid to the applied critical strain values necessary to break the MO and the MI interfaces.

For calculations performed with the highest values of σ_{Ox}^{\max} , no debonding occurs until the applied critical strain for crack formation in the oxide is reached. This result indicates that crack formation in the oxide is a necessary condition to break MO or MI interfaces. On the other hand, low σ_{Ox}^{\max} values do not influence the applied critical strain for MI or MO interface debonding. Crack formation allows relaxing stress in the oxide scale and dissipates the elastic strain energy. Once the critical strain for crack formation is reached, the elastic energy stored in the oxide scale is released. The average stress is lowered but its distribution is no more homogeneous especially high stress concentration grows up in the metal beneath the crack tip. The plastic strain in the metal propagates with increasing loading from the stress concentration zone at crack tip into the bulk and can reach the inclusion. Depending on the properties of the MI interface, inclusion debonding may occur. Investigations performed on the separation energy shows that, as expected, the $G_{c,MI}$ values do not influence the critical strain for initiation of the inclusion debonding but rather the crack growth along the MI interface.

Figures 8 shows the applied critical strain values necessary for inclusion and oxide scale debonding as a function of R , the $\sigma_{MI}^{\max}/\sigma_{MO}^{\max}$ ratio, for distances between inclusion and crack in the oxide of $1.7 \mu\text{m}$ (close crack geometry) and $3.9 \mu\text{m}$ (remote crack geometry). Damage patterns showing the equivalent plastic strain for different values of R for corresponding applied strain of 4% for the close crack geometry and 8% for the remote crack geometry are displayed as insets. For the close crack geometry (Fig. 8a), tractions ratio lower than one favors the inclusion

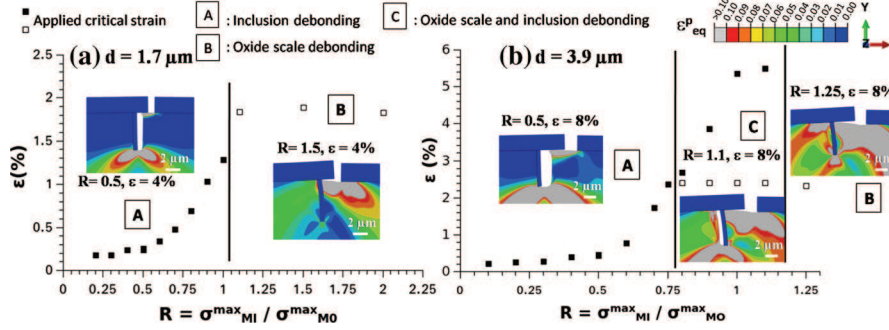


Fig. 8 Evolution of the applied critical strain value as a function of R , the ratio $\sigma_{MI}^{\max}/\sigma_{MO}^{\max}$, for **a** close crack geometry ($d = 1.7 \mu\text{m}$) and **b** remote crack geometry ($d = 3.9 \mu\text{m}$). Insets: equivalent plastic strain

debonding process (A area). The critical strain increases with increasing ratio (full black squares). When the maximum traction necessary to open the MI interface is greater than the one of the MO interface ($R > 1$), damaging behavior changes and decohesion of the oxide scale is favored (empty black squares, B area). The applied critical strain for MO interface debonding remains constant with increasing ratio since only the value of σ_{MI}^{\max} varies in our calculation, σ_{MO}^{\max} remaining constant.

For the remote crack geometry (Fig. 8b), these two behaviors are again observed, with an overlap for intermediate values of R . Single inclusion debonding occurs for ratio lower than 0.8 (A area), whereas single-oxide scale decohesion arises for ratio greater than 1.2 (B area). The transient stage is observed for R varying between 0.8 and 1.2 and is characterized by the decohesion of both interfaces (C area). In this stage, even for $\sigma_{MI}^{\max}/\sigma_{MO}^{\max}$ ratio lower than one (metal/inclusion interface weaker than metal/oxide interface), the traction value near metal/oxide interface can reach the maximum traction value for decohesion for lower critical stress than metal/inclusion interface. It results in a plateau value since σ_{MO}^{\max} is constant in our calculation. Finally, the shape of the curves corresponding to the sole phenomena do not depend on a close or a remote crack geometry. Nevertheless, since the expansion of stress concentration zone from the crack tip to the inclusion requires higher applied strain values for the remote crack geometry than for the close crack geometry, the maximum traction for inclusion debonding is reached for higher applied critical strain value for the former. For a ratio $\sigma_{MI}^{\max}/\sigma_{MO}^{\max} = 1$, applied critical strain is about 5% in the remote crack geometry instead of 1.3% in the close crack geometry.

The simulated damage patterns (insets in Fig. 8) can be compared to the SEM cross section after tensile testing performed on AISI 304L oxidized for 50 h in synthetic air at 900 °C (Fig. 3). It seems that the close geometry configuration associated to value of R lower than one is the most likely. In the experiments first cracks are observed around 4% strain. In the model, the critical strain for inclusion debonding varies from 0.2 to 1.3% (see full black squares curve in Fig. 8a), area A), and at strain around 4% the metal inclusion interface is widely opened (see inset in Fig. 8a): for $R = 0.5$, the opening is about 1 μm). Moreover, in the experiments, the

distance between crack and inclusion is shorter. According to the finite elements calculations, this configuration will lower the applied critical strain for inclusion debonding even more.

This outlines the difficult comparisons between experimental and numerical patterns. The various morphologies of the oxide grains increase the contrast of the surface SEM images making cracks identification more difficult. Moreover, SEM in situ tensile testing experiment focuses on what occurs at the oxide surface and magnification is a compromise between resolution at the scale of the phenomenon to be observed and observation area size large enough to be representative. It is likely that crack formation takes place at lower strain value than observed. SEM observations are more related to the first steps of the crack opening rather than the crack formation. In order to improve the comparison between experiment and simulated patterns, criterion based on applied critical strain values for oxide crack opening would be more relevant.

Conclusion

Tensile testing experiments performed on AISI 304L previously oxidized in synthetic air for 50 h at 900 or 1000 °C have shown that intergranular oxidation of Si plays a key role on the overall damaging behavior of the steel. The accelerated inward interfacial diffusion of oxygen along the grain boundaries promotes the formation of needle-like internal oxides of silica with an increase of particle size with increasing temperature. Crack patterns were linked to the silica embrittlement of the alloy grain boundaries. At 900 °C internal oxidation of silica is discontinuous. When submitted to tensile testing, these small SiO₂ precipitates generate short wavy cracks. At 1000 °C a thin and continuous network of silica forms. During tensile testing, this network induces long chevron-like cracks.

A micromechanical modeling using traction–separation laws to describe interfaces fracture behavior was proposed. Calculations with periodic boundaries conditions were carried out using the finite elements method. One of the investigated parameter was the distance between a transverse crack in the oxide scale and a silica inclusion.

Crack formation in the oxide scale is found to be a necessary condition to break metal/oxide or metal/inclusion interfaces. Crack formation lowers the average stress in the oxide while a high stress concentration zone develops in the metal beneath the crack tip. The expansion of this stress concentration zone from the crack tip to the inclusion requires higher strain values for larger crack/inclusion distance. Investigations performed on the separation energy have shown that the toughness of the metal/inclusion interface does not influence the critical strain for initiation of the inclusion debonding but affects the crack growth. Maximal stress for interface debonding is found to be a key parameter regarding the crack patterns morphology. When the maximum traction necessary to open the metal/inclusion interface is lower (greater) than the one of the metal/oxide interface, decohesion of the inclusion (of the oxide scale) is favored. For the remote crack geometry decohesion, both interfaces are observed for close values of maximum tractions. The damage

morphology after tensile testing observed by SEM cross section appears to be better reproduced by the simulation in the close crack configuration, with values of maximum traction for interface debonding lower for metal/inclusion interface than for metal/oxide interface.

Acknowledgements This work was realized in the framework of a PICS project supported by the National Centre for Scientific Research (CNRS, France) Ref n° 6095 and the Russian Foundation for Basic Research (RFBR, Russia) Ref n° 13-08-91053-CNRS_a.

References

1. H. E. Evans, D. A. Hilton, R. A. Holm, and S. J. Webster, *Oxidation of Metals* **19**, 1 (1983).
2. J. Dunning, D. E. Alman, and J. C. Rawers, *Oxidation of Metals*. **57**, 409 (2002).
3. L. Mikkelsen, S. Linderoth, and J. B. Bilde-Sorensen, *Materials Science Forum*. **461**, 117 (2004).
4. T. Ishitsuka, Y. Inoue, and H. Ogawa, *Oxidation of Metals*. **61**, 125 (2003).
5. G. Bamba, Y. Wouters, A. Galerie, F. Charlot, and A. Dellali, *Acta Materialia*. **54**, 3917 (2006).
6. S. N. Basu and G. J. Yurek, *Oxidation of Metals*. **36**, 281 (1991).
7. N. Birks, G. H. Meier, and F. S. Pettit, *Introduction to the High Temperature Oxidation of Metals* (Cambridge University Press, 2006).
8. E. Fedorova, M. Braccini, V. Parry, C. Pascal, M. Mantel, F. Roussel-Dherbey, D. Oquab, Y. Wouters, and D. Monceau, *Corrosion Science*. **103**, 145 (2016).
9. C. Pascal, V. Parry, E. Fedorova, M. Braccini, P. Chemelle, N. Meyer, D. Oquab, D. Monceau, Y. Wouters, and M. Mantel, *Corrosion Science*. **93**, 100 (2015).
10. F. Toscan, PhD thesis, Institut National Polytechnique de Grenoble, 2004.
11. J. Schindelin, I. Arganda-Carreras, and E. Frise, *Nature methods*. **9**, 676 (2012).
12. M. N. Nagl, W. T. Evans, D. J. Hall, and S. R. J. Saunders, *Oxidation of Metals*. **42**, 431 (1994).
13. D. Lussana, D. Baldissin, M. Massazza, and M. Baricco, *Oxidation of Metals*. **81**, 515 (2014).
14. N. Karimi, F. Riffard, F. Rabaste, S. Perrier, R. Cueff, C. Issartel, and H. Buscail, *Applied Surface Science*. **254**, 2292 (2008).
15. A. L. Ji, W. Wang, and G. H. Song, *Materials Letters*. **58**, 1993 (2004).
16. L. B. Freund and S. Suresh, *Thin Film Materials: Stress, Defect Formation and Surface Evolution* (Cambridge University Press, 2004).
17. A. Needleman, *Journal of Applied Mechanics*. **54**, 525 (1987).
18. K. Park and G. H. Paulino, *Applied Mechanics Reviews*. **64**, 060802 (2013).
19. ABAQUS Manuals Collection. Dassault Systèmes Simulia Corp. Providence, RI, USA, 2010.